actuators

MDPI

Article

A Rotary-Linear Ultrasonic Motor Using MnO_2-Doped $(Ba_{0.97}Ca_{0.03})(Ti_{0.96}Sn_{0.005}Hf_{0.035})O_3$ Lead-Free Piezoelectric Ceramics with Improved Curie Temperature and Temperature Stability

Cheng-Che Tsai [1,*], Sheng-Yuan Chu [2,3,*], Wei-Hsiang Chao [2] and Cheng-Shong Hong [4]

[1] Department of Game and Animation Design, TungFang Design University, Kaohsiung 829, Taiwan
[2] Department of Electrical Engineering, National Cheng Kung University, Tainan 701, Taiwan
[3] Center for Micro/Nano Science and Technology, National Cheng Kung University, Tainan 701, Taiwan
[4] Department of Electronic Engineering, National Kaohsiung Normal University, Kaohsiung 802, Taiwan
* Correspondence: jertsai@seed.net.tw (C.-C.T.); chusy@mail.ncku.edu.tw (S.-Y.C.); Tel.: +886-7-6939627 (ext. 210) (C.-C.T.); Fax: +886-7-6933406 (C.-C.T.); +886-6-2345482 (S.-Y.C.)

Abstract: In this work, a cylindrical lead-free rotary-linear ultrasonic motor was attached to piezoelectric plates of MnO_2-doped $(Ba_{0.97}Ca_{0.03})(Ti_{0.96}Sn_{0.005}Hf_{0.035})O_3$ ceramics using the first bending vibration to pull a thread output shaft of the interior of a stator. The effect of the proposed ceramics' d_{33} and Q_m values are the key factors for ultrasonic motors. Therefore, MnO_2-doped $(Ba_{0.97}Ca_{0.03})(Ti_{0.96}Sn_{0.005}Hf_{0.035})O_3$ lead-free piezoelectric ceramics with high values of d_{33} = 230 pC/N, Q_m = 340.8 and a good temperature stability of their dielectric and piezoelectric properties are suitable for application to linear piezoelectric motors. The structure of the linear piezoelectric motor was simulated and fabricated by Finite Element Analysis. The characteristics of linear piezoelectric motors were also studied. The output characteristics of the lead-free piezoelectric motor were a left-pull velocity = 3.21 mm/s, a right-pull velocity = 3.39 mm/s, an up-pull velocity = 2.56 mm/s and a force >2 N at 39.09 kHz for an input voltage of approximately 200 V_{p-p} (peak to peak). These results are comparable to those for a lead-based piezoelectric motor that uses PZT-4 ceramics. The proposed lead-free piezoelectric motors were successfully fabricated and used to pull a 0.5 mL commercial insulin syringe.

Keywords: lead-free; linear ultrasonic motor; bending vibration; insulin syringes

check for updates

Citation: Tsai, C.-C.; Chu, S.-Y.; Chao, W.-H.; Hong, C.-S. A Rotary-Linear Ultrasonic Motor Using MnO_2-Doped $(Ba_{0.97}Ca_{0.03})(Ti_{0.96}Sn_{0.005}Hf_{0.035})O_3$ Lead-Free Piezoelectric Ceramics with Improved Curie Temperature and Temperature Stability. *Actuators* **2022**, *11*, 248. https://doi.org/10.3390/act11090248

Academic Editor: Katsushi Furutani

Received: 11 August 2022
Accepted: 28 August 2022
Published: 31 August 2022

Publisher's Note: MDPI stays neutral with regard to jurisdictional claims in published maps and institutional affiliations.

Copyright: © 2022 by the authors. Licensee MDPI, Basel, Switzerland. This article is an open access article distributed under the terms and conditions of the Creative Commons Attribution (CC BY) license (https://creativecommons.org/licenses/by/4.0/).

1. Introduction

Motors used for high-precision position detecting or non-electromagnetic mechanical motion are usually made of piezoelectric materials. They use the direct/inverse piezoelectric effect to manufacture devices for diverse applications. Precision machines/instruments for tiny positional movement producing high torque and detecting/sensing articles commonly use linear piezoelectric motors. Motors are categorized into three different types in terms of the different driving modes for their input voltages. A servo motor or DC (Direct Current) motor is driven by rigid replacement under a direct voltage. Because of its strain hysteresis, its material must exhibit high electrostriction, so $Pb(Mg_{1/3}Nb_{2/3})O_3$ (PMN) is used. Servo motors are used in positioners for optical and precision machinery systems. Pulse motors resemble on-off switches. They are driven by induced rigid replacement under a pulse voltage. Pulse motors require a low-permittivity material to give a rapid response with a limited power supply, rather than a small hysteresis, so soft PZT piezoelectric material is suitable for this application. Pulse motors can be used for dot-matrix or ink-jet printers. An ultrasonic motor, or a piezoelectric or AC (Alternating Current) motor, is driven by the resonant replacement of samples under an alternating voltage. Piezoelectric ceramics achieve maximum replacement at their resonant frequency. A complete ultrasonic motor includes piezoelectric material, a stator, a frictional material

and a slider or rotor. The slider or rotor is rotated or moved linearly by the movement of the stator due to tiny displacement of the piezoelectric material. The material that is used to fabricate an ultrasonic motor must have a high quality factor and low dielectric loss for the piezoelectric material, such as PZT-4 and PZT-8 [1,2].

Compared with conventional electromagnetic motors, ultrasonic motors (Piezoelectric motors) have great advantages, such as high efficiency for miniature motors, freedom from electromagnetic interference, the lack of a need for additional gears, high output torque at low speed, high resolution for accurate displacement control, instant braking for the power-off stage due to friction between the stator and the slider and a quick response to the driving electric signal [3,4]. Valuable papers were presented by the research teams for piezoelectric motors [5–8].

The first rotary piezoelectric motor that used wobbling was invented by A.L.W. Williams and W.J. Brown in 1948 [9]. This motor used an orbiting stator (a lead screw slide) to engage a round shaft to produce rotation by tangential contact. Afterwards, a miniature patented piezoelectric linear motor from New Scale Technologies used ultrasonic standing wave vibrations in a threaded nut to directly rotate a screw through friction and simultaneously translated this rotation into linear motion. The nut vibration is described as a "hula hoop", wobble or orbiting motion. A squiggle motor has (1) a high-output linear force; (2) a reducing linear speed; (3) sub-micrometer stepping; and (4) precise off-power holding and velocity control. It can be applied in different fields, such as for microfluidic devices, insulin syringes, drug delivery during MRI, auto focus systems for cameras and deformable mirrors for adaptive optics [10–12]. A rotary-linear ultrasonic motor with a designed-thread output shaft, which was of the same type as the squiggle structure, was used for this study.

The property requirements for piezoelectric materials that are used for squiggle motors are (1) a high piezoelectric constant to generate greater vibration of the piezoelectric plates; (2) a high quality factor (Q_m) to delay heat generation at high voltages; (3) low dielectric loss; (4) high density; and (5) a small grain size.

Among the different piezoelectric materials, lead-based piezoelectric ceramics are widely used in sensors, ultrasonic motors and transformers, but they can pollute the environment and damage the nervous system of human beings because of the toxicity of the lead vapor produced during the sintering process [13]. Lead-free piezoelectric materials [14,15] which are anticipated to replace lead-based piezoelectric materials, are classified into four different compositions: (K,Na)NbO_3 (KNN) [14–16], (Bi,Na)TiO_3 (BNT) [17–20], (Ba,Ca)(Ti,Zr)O_3 (BCTZ) [21–23] and (Ba,Ca)(Ti,Sn)O_3 (BCTS) [24–29] lead-free piezoelectric ceramics. One of the alternatives to lead-based materials is (K,Na)NbO_3 (KNN). Despite the fact that KNN ceramics have a higher Curie temperature of T_C = 400–450 °C and better temperature stability than PZT ceramics, there is some volatile loss of the alkali ions during the high-temperature sintering process. Nonstoichiometry also occurs, and there is a departure from the initial stoichiometric ratio, resulting in decreasing piezoelectric properties. Therefore, it is difficult to synthesize high-density KNN ceramics. Another alternative lead-free piezoelectric ceramic is (Bi,Na)TiO_3 (BNT). Although BNT ceramics also have a higher Curie temperature of T_c = 320 °C and are strongly ferroelectric, there is also some volatile loss of bismuth and sodium during the high-temperature sintering process, so the piezoelectric properties deteriorate, and these have the same shortcomings as KNN ceramics. It is also difficult to the make domains of BNT ceramics rotate easily during the poling process because of the high coercive field and the high conductivity of BNT ceramics, which is not beneficial to the piezoelectric properties. Some studies have seen that (Ba,Ca)(Ti,Zr)O_3 (BCTZ) and (Ba,Ca)(Ti,Sn)O_3 (BCTS) ceramics may be possible successors to lead-based piezoelectric ceramics because of their high piezoelectric properties, high density and low dielectric loss by tuning the Zr or Sn content.

The disadvantages of BCTZ and BCTS ceramics include their high sintering temperature (>1450 °C), low Curie temperature T_C (<100 °C) and low temperature stability of their piezoelectric coefficients. These are disadvantageous for practical applications. In this work, BCTS-based ceramics were chosen as the piezoelectric material to improve the piezoelectric

properties (good d_{33} > 230 and Q_m > 300), temperature stability (decreased by 20% of the original values in the temperature ranges of 20–90 °C) and high Curie temperature (T_c > 120 °C). Linear piezoelectric motors are fabricated using these materials for the study of piezoelectric motors [30–33]. The material properties of BCTS-based ceramics are more suitable for linear piezoelectric motors than ones using the other lead-free piezoelectric materials, such as NKN or BNT-based materials. To the best of the authors' knowledge, lead-free BCTS-based piezoelectric ceramics have never been applied in ultrasonic motors and this is the motivation for this study.

This study is a continuation of previous work by the authors [34]. This study showed a two-stage modification of $(Ba_{0.97}Ca_{0.03})(Ti_{0.96}Sn_{0.04})O_3$ (BCTS), $(Ba_{0.97}Ca_{0.03})(Ti_{0.96}Sn_{0.005}Hf_{0.035})O_3$ (BCTSH), which has a high curie temperature and excellent temperature stability and MnO_2-doped $(Ba_{0.97}Ca_{0.03})(Ti_{0.96}Sn_{0.005}Hf_{0.035})O_3$ (BCTSH + Mn), which has a high quality factor and good temperature stability for its piezoelectric coefficients, and simultaneously increases the Curie temperature. This study used three different types of piezoelectric ceramics (soft BCTSH, hard BCTSH + Mn and commercial PZT-4 ceramics) to fabricate rotary-linear ultrasonic motors. The output performance of the BCTSH + Mn- and PZT-4-based devices were simulated and measured. The output force and velocity of the ultrasonic motors were also studied to determine the correlation between the piezoelectric constant, the quality factor and the motors' output characteristics. In addition, the rotary-linear ultrasonic motors using BCTSH + Mn ceramics could generate enough force to pull a 0.5 mL commercial insulin syringe as compared to those using PZT ceramics.

2. Materials and Methods

2.1. Material Synthesis

The lead-free BCTS, BCTSH and BCTSH + Mn piezoelectric ceramics were prepared using a conventional solid state reaction method. In this conventional solid state reaction method, the BCTSH ceramics were prepared using pure oxides of $BaCO_3$, $CaCO_3$, TiO_2, SnO_2 and HfO_2 powders (>99% purity) as raw materials. The $BaCO_3$, $CaCO_3$, TiO_2, SnO_2, and HfO_2 powders were ball-milled in a polyethylene jar for 12 h using ZrO_2 balls and anhydrous ethanol (>99.5% purity) as the medium. After drying, the powders were calcined at 1150 °C for 4 h at a heating rate of 5 °C/min in air. MnO_2 powders were then added into the BCTSH precursors, according to the stoichiometric formula for BCTSH + Mn, and ball-milled together for 24 h. After drying, the BCTSH + Mn powders were mixed with 13 wt% polyvinyl alcohol (PVA) aqueous solution and filtered using a 120-mesh sieve and then pressed into 10 mm diameter and 1.2 mm thick discs. These disc samples then underwent binder burnout at 650 °C for 3 h at a heating rate of 5 °C/min in air. Finally, all of the specimens were sintered at 1350 °C for 2 h at a heating rate of 5 °C/min in air.

The crystalline profile was determined using X-ray diffraction (XRD) with CuKα (λ = 0.15406 nm) radiation, using a MultiFlex X-ray diffractometer (Rigaku Corp., Tokyo, Japan). To confirm the exact diffraction angles, silicon powders were used for calibration. The phase structure analysis was performed using the Rietveld-Method with TOPAS software. The microstructure of the samples was seen using an S-4100 (Hitachi Ltd., Tokyo, Japan) scanning electron microscope (SEM). The average grain size (AGS) was calculated using the linear intercept method. The bulk densities were measured using the Archimedes method. Silver paste was applied to both sides of the 1 mm thick polished samples to serve as electrodes. After drying at 120 °C in an oven, the silver electrodes were pasted on the top and bottom surfaces of the sintered samples and then poled using a dc field (30 kV/cm) at room temperature for 20 min in a silicone oil bath. The dielectric properties were measured using an HP 4294A precision impedance analyzer (Agilent Technologies Inc., Santa Clara, CA, USA) and the piezoelectric constant was measured using an APC 90–2031 d_{33} m (APC International Ltd., Mackeyville, PA, USA). The electromechanical coupling factor for the planar (k_p), the longitudinal (k_{33}), the transverse (k_{31}) and the mechanical quality factor (Q_m) were calculated using the resonance and anti-resonance method. The Ferroelectric properties (Polarization-Electric field loops) and the piezoelectric charge constant d_{33} were

measured using a Radiant Precise Workstation (Radiant Technologies, Medina, NY, USA) with a fiber optic displacement sensor (MTI-2100 Fotonic Sensor, MTI Instruments, Inc., Albany, NY, USA) at a frequency of 1 Hz. The piezoelectric properties were determined as a function of temperature using an impedance analyzer and a temperature-controlled oven.

2.2. Finite Element Analysis (FEA)

The output performance of the piezoelectric motors using the BCTSH + Mn (with Q_m of 350) piezoelectric ceramic plates were simulated. The BCTSH + Mn piezoelectric material properties matrices are as follows:

$$s^E = \begin{bmatrix} 8.55 & -2.61 & -2.85 & 0 & 0 & 0 \\ -3.76 & 8.55 & -2.85 & 0 & 0 & 0 \\ -2.85 & -2.85 & 8.95 & 0 & 0 & 0 \\ 0 & 0 & 0 & 23.3 & 0 & 0 \\ 0 & 0 & 0 & 0 & 23.3 & 0 \\ 0 & 0 & 0 & 0 & 0 & 22.1 \end{bmatrix} \times 10^{-12} \frac{m^2}{N} \quad (1)$$

$$d = \begin{bmatrix} 0 & 0 & 0 & 0 & 340 & 0 \\ 0 & 0 & 0 & 340 & 0 & 0 \\ -80 & -80 & 240 & 0 & 0 & 0 \end{bmatrix} \times 10^{-12} \frac{\mathrm{C}}{\mathrm{N}} \quad (2)$$

$$\frac{\varepsilon^T}{\varepsilon_0} = \begin{bmatrix} 1610 & 0 & 0 \\ 0 & 1610 & 0 \\ 0 & 0 & 1620 \end{bmatrix}, \ \varepsilon_0 = 8.854 \times 10^{-12} \frac{\mathrm{F}}{\mathrm{m}} \quad (3)$$

The performances of the motors were simulated and designed using the Workbench interface of the ANSYS finite element software. Due to the different characteristic matrices of the input, Equations (1)–(3) need to be converted to fit the e-form of the piezoelectric equation (Equations (4) and (5)):

$$\mathrm{T} = \mathrm{c}^{\mathrm{E}}\mathrm{S} - \mathrm{eE} \quad (4)$$

$$\mathrm{D} = \mathrm{eS} + \varepsilon^S \quad (5)$$

where

$$c^E = \left[s^E\right]^{-1}$$

$$e = \left[s^E\right]^{-1}[d]$$

$$\varepsilon^S = \varepsilon^T - [d]^t\left[s^E\right]^{-1}[d]$$

The model of the piezoelectric motor established using ANSYS after the conversion of the piezoelectric material parameters using Equations (1)–(5) is shown in Figure 1. The optimum dimension of the rotary-linear motor was simulated. The piezoelectric ceramic plates were 30 mm × 8 mm × 1 mm and glued to each of the four sides of the stator using epoxy resin. The stator had dimensions of 30 mm × 8 mm × 8 mm in the form of a hollow cylinder with an inner diameter of 4 mm. The diameter of the threaded shaft was 4 mm, and the length was 75 mm. The stator and shaft were both made of medium-carbon steel. The opposing pairs of piezoelectric plates shared the same polarization direction.

2.3. The Fabrication of the Piezoelectric Element and the Squiggle Motor

The configuration of the linear squiggle motors was designed through finite element analysis using the ANSYS software in this work. Figure 1a,b show photos of the proposed stator and the squiggle motor with a threaded output shaft. The dimensions of the proposed stators were 30 mm × 8 mm × 8 mm cuboids with inner diameters of 4 mm for the hollow cylinders and the stators were affixed using four piezoelectric plates with a thickness of 1 mm. The diameter and length of the threaded shafts were 4 mm and 75 mm, respectively. The piezoelectric plates were 30 mm × 8 mm × 1 mm. The material for the stator and shaft

was medium-carbon steel and brass. The piezoelectric plates were pressed from calcined powders with 13 wt % PVA binder using a molding press. The rectangular samples then underwent binder burnout at 650 °C for 3 h at a heating rate of 5 °C/min in air. Finally, all of the samples were sintered at 1350–1400 °C for 2 h at a heating rate of 5 °C/min in air. The sintered ceramics were polished to a thickness of 1 mm using a surface-polishing machine. Silver paste was applied on both sides of the 1 mm thick polished plates to serve as electrodes. After drying at 750 °C using for 10 min in a furnace, silver electrodes were pasted on the top and bottom surfaces of the sintered samples and then poled using a dc field (30 kV/cm) at room temperature for 20–30 min in a silicone oil bath. The four poled piezoelectric plates were bonded to the four flat surfaces of the stator using thermosetting for epoxy resin at 70 °C for 16 h. The polarization direction for the two piezoelectric plates on opposite surfaces of the stator was the same. Two wires were then separately connected to the two pairs of opposite surfaces of the piezoelectric plates to create two pairs of opposite piezoelectric plates in parallel and another two wires were connected to the two orthogonal surfaces of the piezoelectric plates to input two voltage signals with a 90° phase shift. The last wire was connected to the metal of the stator as a ground connection. To allow measurement of the motor's performance, a fixture clipped to the node of the squiggle motor at one quarter of the length of the piezoelectric plate. The wire was bonded to the piezoelectric plate using sliver paste at 70 °C for 3 h. The piezoelectric plates were glued to the stator (hollow cylinder) using epoxy resin at 65 °C for 10 h.

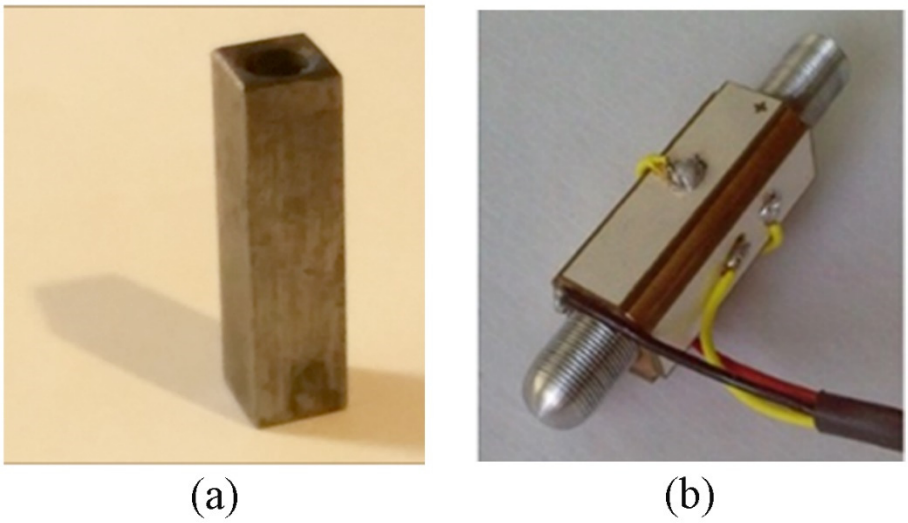

Figure 1. A diagram of (**a**) a stator having a 30 mm × 8 mm × 8 mm cuboid shape with an inner diameter of 4 mm for the hollow cylinder and (**b**) a squiggle motor with a threaded output shaft and four piezoelectric plates with 30 mm × 8 mm × 1 mm (thickness) being affixed the stator. The diameter and length of the threaded shafts were 4 mm and 75 mm, respectively.

After the squiggle motors were assembled, the output characteristics were measured. The measurement system will be discussed in the next section.

3. Results and Discussion

3.1. Microstructure and the Electrical Properties of BCTS, BCTSH and Mn-Doped BCTSH Ceramics

Figure 2 shows the XRD patterns for the BCTS, BCTSH and Mn-doped BCTSH ceramics. All the samples had a Perovskite structure without any secondary phases. The diffraction peak at around 45° did not change when HfO_2 was substituted for SnO_2 because Sn^{4+} (0.71 Å) and Hf^{4+} (0.71 Å) have a similar ionic radius. However, the diffraction peaks at around 45° also gradually shifted to a high angle with the addition of MnO_2 for BCTSH ceramics, which demonstrates that doping with MnO_2 changed the structure of the BCTSH ceramics because the ionic radii of Mn^{4+} (0.53 Å) and Mn^{3+} (0.70 Å) possibly entered the

B-site of crystal structure to replace the Ti^{4+} (0.61 Å), Sn^{4+} (0.72 Å) and Hf^{4+} (0.72 Å), resulting in a lattice of crystal structure contraction. It has been reported that Mn ions can exist as Mn^{+2} or Mn^{+3} if MnO_2-doped samples are sintered at a temperature of 1450 °C [35]. However, the BCTSH + Mn ceramics that were sintered at 1350 °C in this study had the ion form of Mn^{+4} or Mn^{+3}, instead of Mn^{+2}, because of the lower sintering temperature.

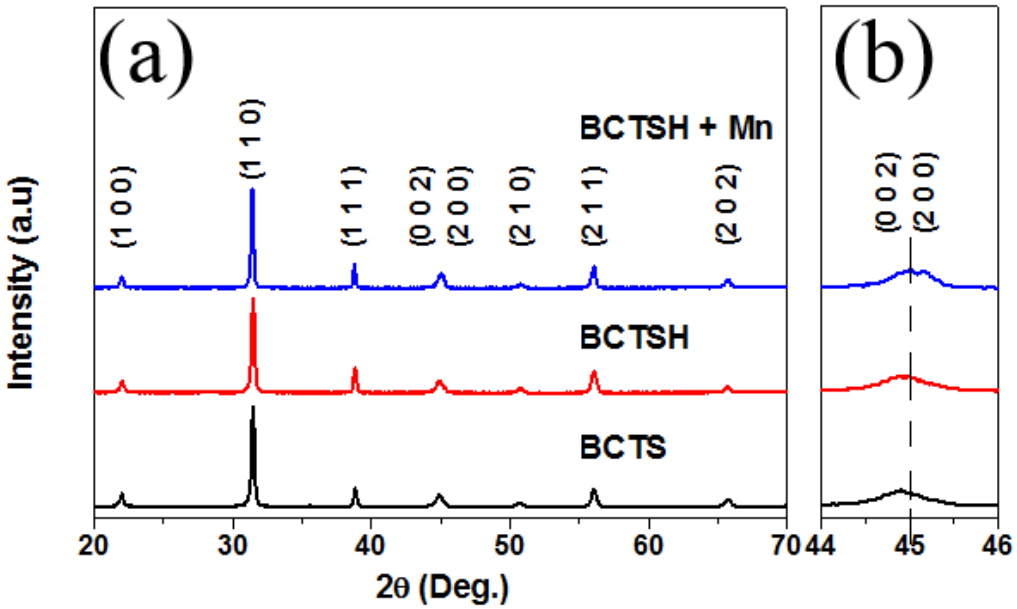

Figure 2. (**a**) XRD patterns and (**b**) Enlarged patterns in the range of 44–46 degrees for BCTS, BCTSH and Mn-doped BCTSH ceramics.

Figure 3a–c show the SEM images for the BCTS, BCTSH and BCTSH + Mn ceramics. It can be seen that the grain size decreased significantly from 83.52 µm (BCTS) and 62.96 µm (BCTSH) to 22.59 µm (BCTSH + Mn) (see Figure 3d). Fine-grained ceramics are best for a device that is driven at a high voltage because the mechanical loss from friction between fine-grained ceramics is less than that for coarse-grained ceramics [36,37].

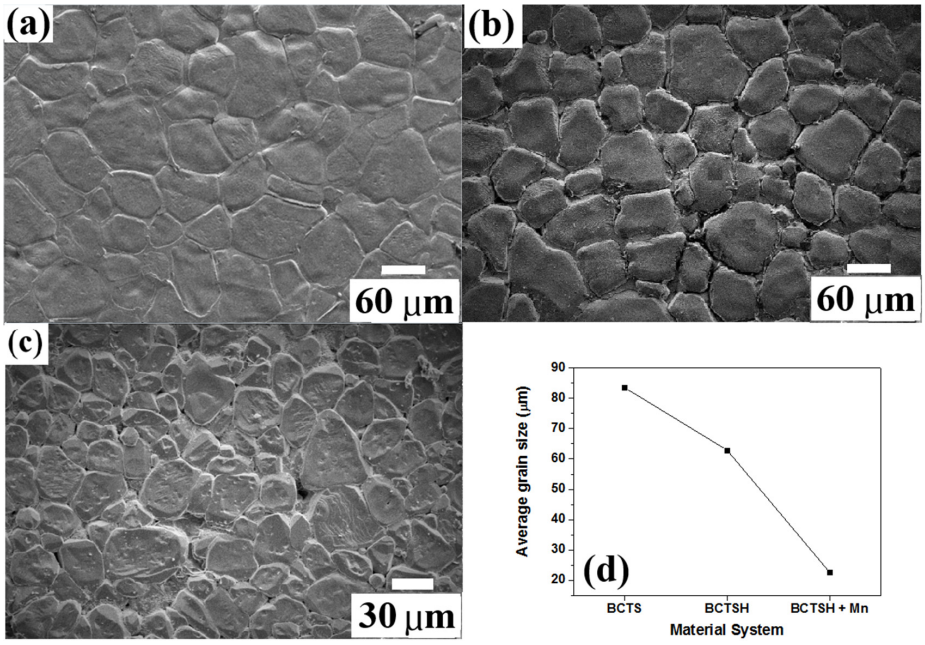

Figure 3. SEM images for (**a**) BCTS, (**b**) BCTSH, (**c**) Mn-doped BCTSH ceramics; (**d**) The average grain size of all proposed samples.

Figure 4 shows the effect of temperature on the permittivity of the BCTS, BCTSH and BCTSH + Mn ceramics. It can be seen that the BCTSH + Mn ceramics had a dielectric constant that was more stable to temperature variations than that of the BCTS and BCTSH. This indicates that the capacitance was insensitive to the temperature variation, and it was easy to match the inductance-capacitive power circuit to generate a steady driving frequency for the squiggle motors.

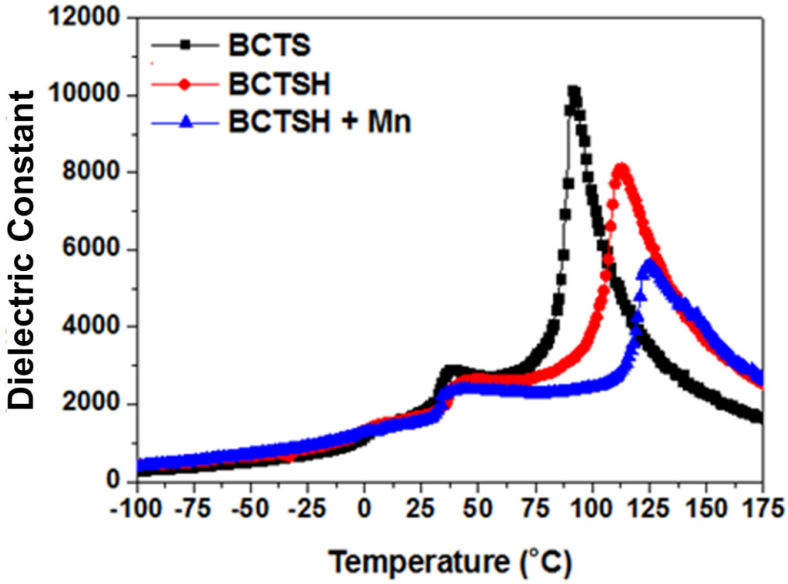

Figure 4. Temperature dependence of the dielectric constant at a measurement frequency 100 kHz for BCTS, BCTSH and Mn−doped BCTSH ceramics.

Figure 5 shows the temperature stability measurement for the thermal aging d_{33} of the BCTS, BCTSH and BCTSH + Mn ceramics. It can be seen that the BCTSH and BCTSH + Mn ceramics improved the thermal aging of the piezoelectric properties because the Curie temperature (T_C) increased, so that the de-poling temperature (the temperature of piezoelectric coefficients decreasing to 20% of original values) correspondingly increased. Interestingly, the thermal d_{33} aging rate for the BCTSH + Mn ceramics was lower than that for the BCTS and BCTSH with temperature up to 110 °C because the $T_{O\text{-}T}$ was increased towards the high temperature.

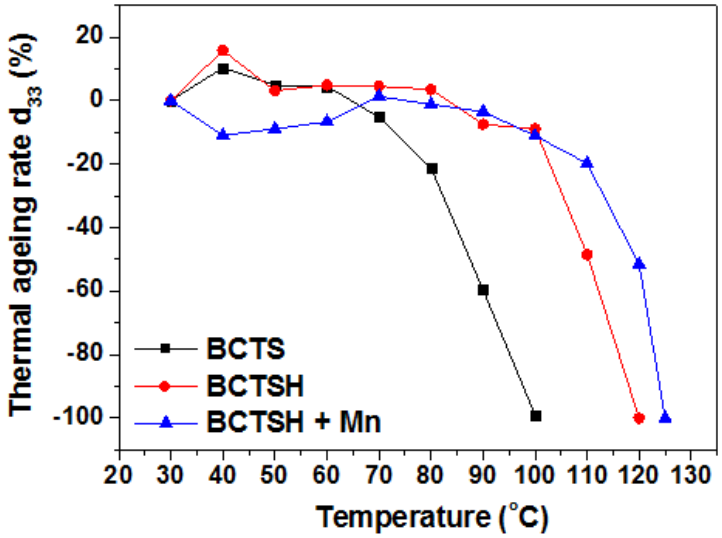

Figure 5. Temperature stability measurement for the thermal aging d_{33} of BCTS, BCTSH and BCTSH + Mn ceramics.

Figure 6 shows the bipolar strain-electric field (S−E) loops for the BCTS, BCTSH and BCTSH + Mn ceramics at 10 kV/cm and 1 Hz at room temperature. All of the samples exhibited butterfly-shaped S–E loops that are normal for ferroelectric materials. Generally speaking, the butterfly-shaped strain loops that are caused by an AC electric field in ferroelectric ceramics are attributed to both intrinsic and extrinsic contributions. The intrinsic contribution is mostly related to the variation in the lattice distortion. A general way to improve the intrinsic contribution used to be to adjust the chemical compositions within the multiple coexisting ferroelectric phases, which effectively improves the polarization rotation and extension [38–40]. The extrinsic contribution of strains is mainly from switching the domain, which is aligned along the direction of the applied electrical field. It is reported that a high d_{33} piezoelectric material can generate relatively high strain, so the BCTS and BCTSH ceramics had a relatively larger strain of 0.22% and 0.20%, due to the coexistence of two or three ferroelectric phases and a higher P_r value than that of the BCTSH + Mn ceramics and a lower P_r value. The BCTSH + Mn ceramics had a smaller value than that for the BCTS or BCTSH because the BCTSH + Mn ceramics generated more defect dipoles because oxygen vacancies were produced for valence balance. The domain wall motion was restricted and the extrinsic contribution for strain versus an electric field was decreased.

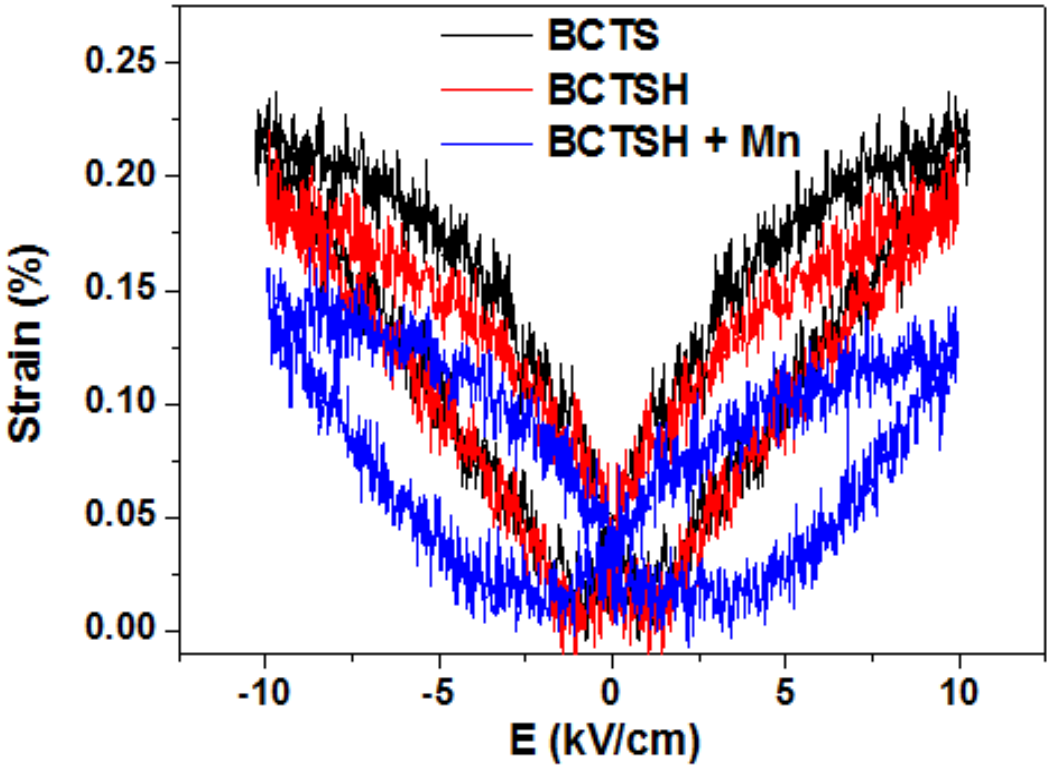

Figure 6. Bipolar strain-electric field (S−E) loops for BCTS, BCTSH and BCTSH + Mn ceramics.

Table 1 shows the detailed material properties of the BCTS, BCTSH and BCTSH + Mn ceramics. The Hf-Modified BCTS had a higher Curie temperature and electrochemical coupling value, k, but a slightly lower piezoelectric charge coefficient. The addition of Hf also increased the de-poling temperature and increased temperature stability of the piezoelectric properties. Therefore, the soft characteristics were improved by the addition of Hf. When Mn was doped into BCTSH (BCTSH + Mn), the Q_m value and the temperature stability were enhanced because defect dipoles were created, and the Tc value (Curie temperature) increased. There was a corresponding increase in the de-poling temperature. Therefore, the addition of Hf and Mn improved the "soft" and "hard characteristics" and the temperature stability of the piezoelectric parameters was also improved.

Table 1. The material properties of BCTS, BCTSH and BCTSH + Mn ceramics.

Property	BCTS	BCTSH	BCTSH + Mn
Density (g/cm^3)	5.8	5.7	5.8
k_p (%)	0.435	0.49	0.364
k_{31} (%)	0.25	0.29	0.21
d_{33} (pC/N)	383	313	230
d_{31} (pC/N)	−88.7	−71.6	−52
Q_m	107.5	122.4	340.8
Resonant impedance R_Z (Ω)	17.25	19.65	14.15
$\varepsilon_{33}^T/\varepsilon_0$ (at 1 kHz)	3728.4	2131.2	1895.7
Tanδ (at 1 kHz)	0.026	0.027	0.024
θ (polarizing angle)	83	86	86
$T_{O\text{-}T}$ (°C)	40	50	44
T_C (°C)	97	112	123

3.2. Measurement of the Output Characteristics of Lead-Free Piezoelectric Motors

In order to understand the performance of the lead-free piezoelectric motor using the BCTSH + Mn (with Q_m of 350) piezoelectric ceramic plates, the model in Figure 7a was used to analyze the vibration mode. The simulation results showed the resonant frequency of the piezoelectric motor using the ANSYS software. The resonance mode of this motor is shown in Figure 7b (Bending up and down) and Figure 7c (Bending left and right). The first resonant frequency of the motor was about 41.3 kHz (see Figure 8a), which is the result of simulation with ANSYS. Moreover, the simulation results also show that there was a large displacement in the x and y directions when the motor was operated at 41.3 kHz. Figure 8b presents the impedance of the piezoelectric motor modeled on the first bending mode using ANSYS Harmonic Response. The piezoelectric motor was measured using an impedance analyzer in order to verify the accuracy of its simulation. In the measurement of the lead-free piezoelectric motor, the first resonant mode frequency was 39.23 kHz. The resonance frequency had a slight difference between the measurements and the simulation due to the errors caused by the manufacturing process (such as glue adhesion, the size and position of the soldier point on the ceramics plate, etc.) and involved the piezoelectric coefficient value in the simulation.

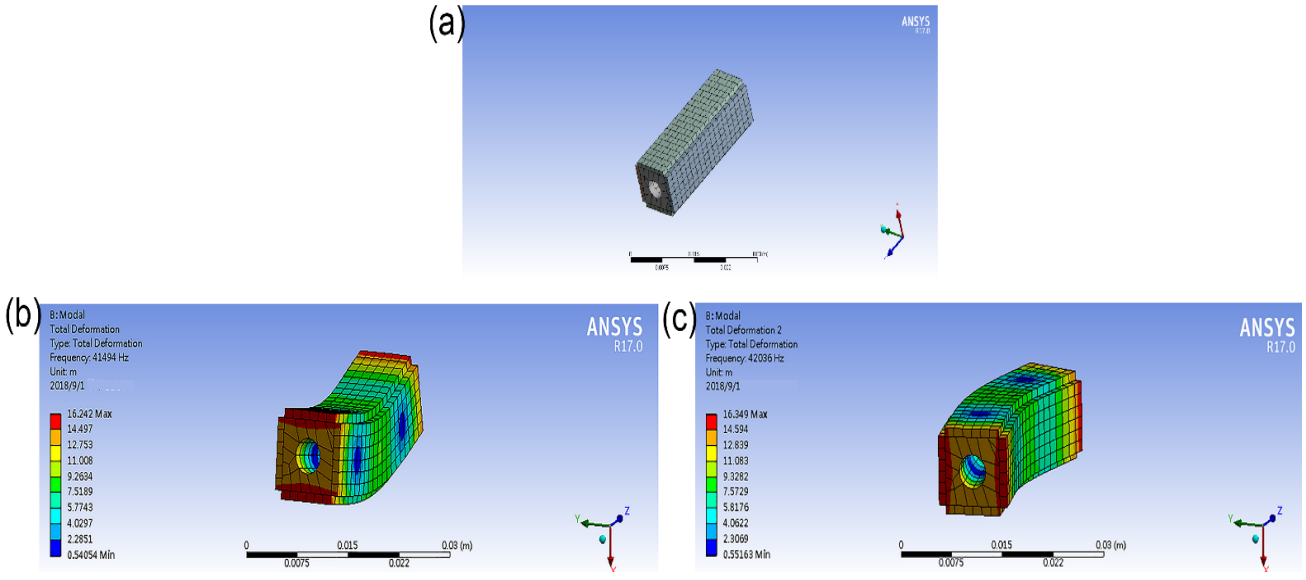

Figure 7. (**a**) The model of piezoelectric motor established by ANSYS (**b**) Bending up and down (**c**) Bending left and right of lead-free piezoelectric motor.

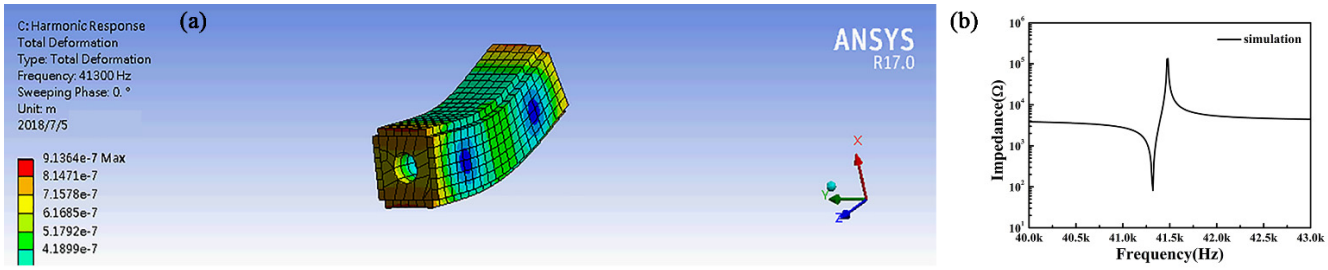

Figure 8. (**a**) The bending simulation result of lead-free piezoelectric motor using ANSYS software; (**b**) The first resonant frequency of lead-free piezoelectric motor with ANSYS Harmonic Response.

In order to gain evidence of the simulation results of the piezoelectric motors, the measured results of the piezoelectric motors in our work were practiced. Figure 9 shows a measurement system that used the Agilent 4294A impedance analyzer (Hewlett-Packard, Palo Alto, California) to detect two resonant frequencies from two pairs of piezoelectric plates in parallel. The average of these two resonant frequencies was the driving frequency for the squiggle motor. It shows the entire measurement system for a squiggle motor. The squiggle motor was driven by an FG-708S function generator with two channels, which generated two voltage signals from 40 V_{pp} to 200 V_{pp} with a 90-degree phase difference (Motech Industries Inc., Taipei, Taiwan), and two BA4825 high-speed bipolar amplifiers (NF Corporation, Yokohama, Japan). A LK-G5000 laser Doppler displacement meter (Keyence Corporation, Taipei, Taiwan) measured the velocity of the squiggle motor. A container with weights was mounted on the top of shaft using nuts and measured the output force from the squiggle motor. The output power from the squiggle motor was the product of the output velocity and the force. The voltage, current and power at the input section were measured using a TCP A300 current probe (Tektronix Inc., Beaverton, State of Oregon) and a Tektronix DPO 2024 digital oscilloscope. The temperature rise in the squiggle motor was measured by an infrared thermometer and the measurement location was at the center of the piezoelectric plate. A commercial 0.5 mL insulin syringe was mounted on the magnetic holder, which was fixed on the optical table. The squiggle motor was also fixed using a customized stage on the optical table. Both the squiggle motor and the insulin syringe were at the same height.

Three different piezoelectric ceramic plates, which were a commercial lead-contained piezoelectric plates (PZT-4) and the lead-free BCTSH and BCTSH + Mn piezoelectric plates, were used to fabricate the squiggle motors and the output characteristics for these motors were measured. Table 2 shows the magnitude of the impedance and phase spectra for the PZT-4, BCTSH and BCTSH + Mn piezoelectric motors, as measured using an impedance analyzer. The measured resonance frequencies for the two pairs of piezoelectric plates in parallel for the PZT, BCTSH and BCTSH + Mn piezoelectric motors were 36.79 kHz, 32.11 kHz and 39.23 kHz, for electrode pair A-A, respectively, and 36.98 kHz, 32.17 kHz and 38.95 kHz, for electrode pair B-B, respectively.

Table 2. The resonant frequencies and impedance of PZT, BCTSH and BCTSH + Mn piezoelectric motors using impedance analyzer.

Material	PZT		BCTSH		BCTSH + 2 Mn	
f_r (kHZ)	A: 36.07	B: 36.20	A: 32.11	B: 32.17	A: 39.23	B: 38.95
f_a (kHZ)	A: 36.67	B: 37.02	A: 32.50	B: 32.47	A: 39.55	B: 39.40
Driving Frequency (kHZ)	A: 36.13	B: 36.13	A: 32.14	B: 32.14	A: 39.09	B: 39.09
Z (Ω)	A: 604.8	B: 711	A: 254.63	B: 195.97	A: 423.8	B: 437.1

A represents the resonant and antiresoant frequencies of one pair of two rectangular piezoelectric sheets on opposite surfaces; B represents the resonant and antiresoant frequencies of the other pair with the same structure of A one.

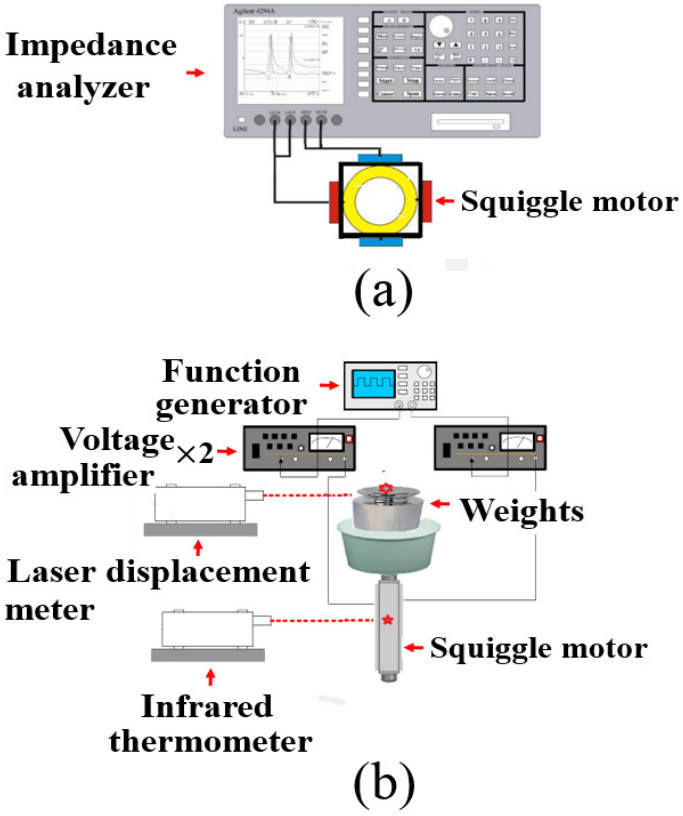

Figure 9. (**a**) The Agilent 4294A impedance analyzer measurement for the phases and resonant frequencies of A and B pairs of ceramics sheets for the rotary linear motor and (**b**) the whole measurement system of rotary linear motor.

The impedance of the piezoelectric motor modeled on the first bending mode using ANSYS Harmonic Response was as shown in the previous section (shown in Figure 8). We measured the piezoelectric motor using an impedance analyzer in order to verify the accuracy of its simulation. In the measurement of the piezoelectric motor, the first resonant mode frequency was 43.8 kHz. The resonance frequency had a slight difference between the measurement and the simulation due to the error caused by the manufacturing process.

Figure 10a,b show the relationship between the left-pull and right-pull speed of the PZT, BCTSH and BCTSH + Mn piezoelectric motors using the two–phase driving voltage amplitude, and these were measured at their driving frequencies. The measurements show that the piezoelectric motors moved toward the left when the phase difference between the two–phase voltages was $+\pi/2$ or $-\pi/2$. The driving frequencies for the PZT, BCTSH and BCTSH + Mn piezoelectric motors were 36.88 kHz, 32.14 kHz and 39.09 kHz, respectively. The thickness of the piezoelectric plates was 1 mm. Interestingly, the speed of the traveling-wave in the lead-free BCTSH piezoelectric motors varied almost linearly with the driving voltage, within a voltage range from 50 $V_{P\text{-}P}$ to 150 $V_{P\text{-}P}$. The optimum driving voltage was 150 V_{PP}. The BCTSH piezoelectric motors had a maximum left-pull and right-pull speed of 3.12 mm/s and 3.12 mm/s at the optimum driving voltage of 150 $V_{P\text{-}P}$. It is worth noting that the left-pull and right-pull speed of the BCTSH piezoelectric motors decreased at a driving voltage of 200 $V_{P\text{-}P}$ because the BCTSH piezoelectric ceramics had a low mechanical quality factor (Q_m = 122.4) and experienced a large mechanical loss. This led to a quick rise in temperature at a high driving voltage and then the piezoelectric coefficients deteriorated (such as piezoelectric charge coefficient *d*, resonant resistance etc.) in the bending modes [41–43]. However, the left-pull and right-pull speed of the PZT-4 and BCTSH + Mn piezoelectric motors almost linearly increased as the driving voltage increased to 200 $V_{P\text{-}P}$, because the PZT-4 and BCTSH + Mn ceramics had a higher Q_m and smaller average grain size than those of the BCTSH ceramics. The higher the Q_m of a piezoelectric

material, the less heat is generated inside the ceramics and the lesser the friction between smaller grains. The mechanical losses for the PZT-4 and BCTSH + Mn ceramics with small grain sizes were less than that with larger grains for the BCTSH ceramics at a high driving voltage [34,35]. The optimum driving voltage for PZT-4 and BCTSH + Mn ceramics was more than 200 V_{P-P}. The PZT-4 and BCTSH + Mn piezoelectric motors had a respective maximum left-pull and right-pull speed of 3.84 mm/s and 3.74 mm/s, and 3.21 mm/s and 3.39 mm/s at a driving voltage of 200 V_{P-P}.

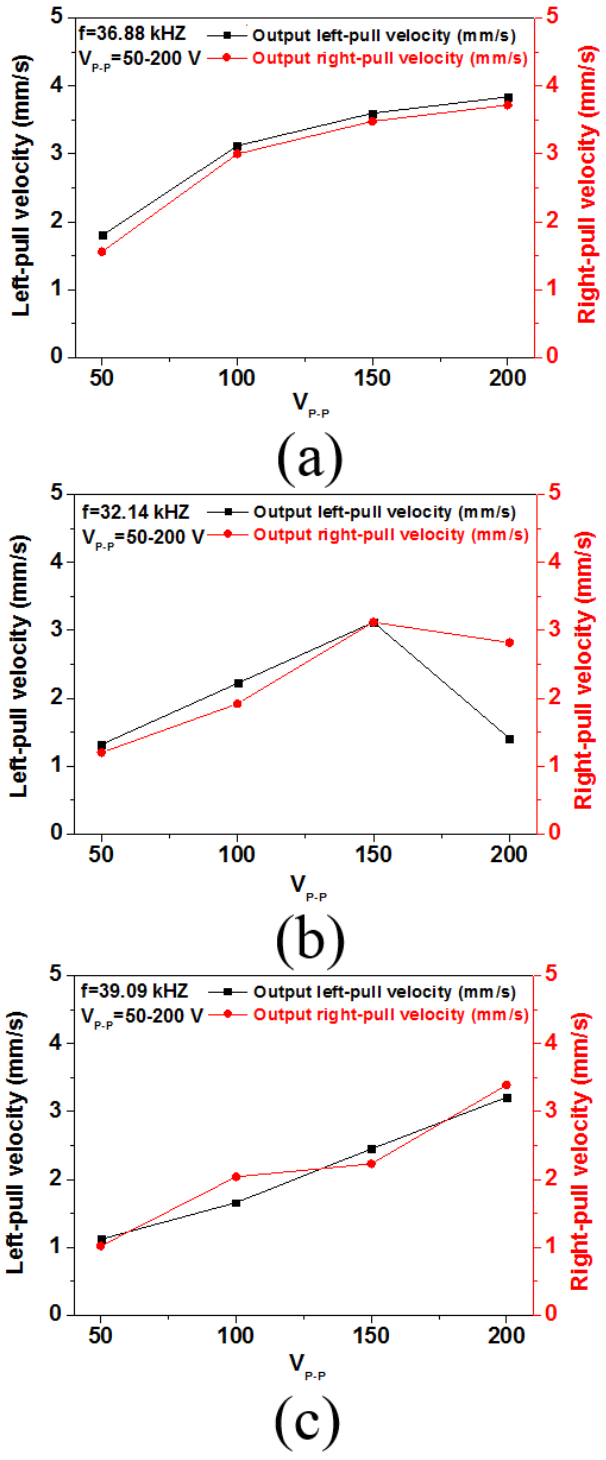

Figure 10. The relationship between the leftward and rightward speed of the (**a**) PZT, (**b**) BCTSH and (**c**) BCTSH + Mn piezoelectric motors using a two−phase driving voltage amplitude, as measured at their driving frequencies.

Figure 11 shows the temperature rise, ΔT, in the BCTSH, PZT-4 and BCTSH + Mn piezoelectric motors after 5 min at a driving voltage of 150 V_{P-P}. The BCTSH + Mn piezoelectric motors exhibited a lower temperature rise after 5 min than BCTSH- and PZT-4-based piezoelectric motors. Piezoelectric motors must work at the resonant frequencies of the piezoelectric ceramics at a high driving voltage. A high Q_m value for a piezoelectric material is required to prevent fluctuation in the driving frequencies due to heat generation. A hard piezoelectric material is suitable for use in ultrasonic motors.

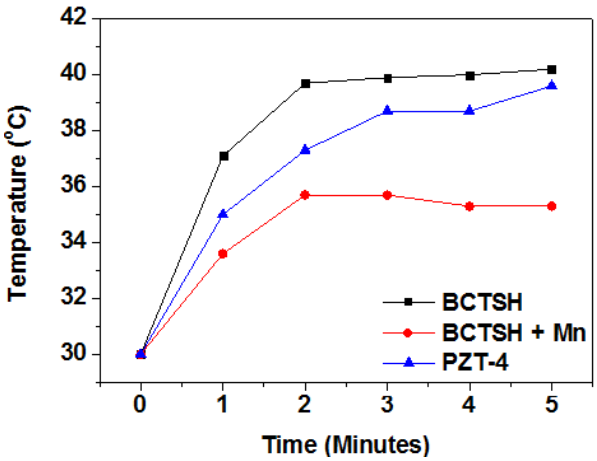

Figure 11. The rise in temperature, ΔT, for BCTSH and BCTSH + Mn piezoelectric motors after 5 min at a driving voltage of 150 V_{P-P}.

Figure 12a,b show the relationship between the up-pull speed, force and output power for the PZT-4 and BCTSH + Mn piezoelectric motors and the two–phase driving voltage amplitude, as measured at the driving frequencies. The measurements show that the piezoelectric motors moved upward and downward when the phase shift of the voltages was between $+\pi/2$ and $-\pi/2$. The driving frequencies for the PZT-4, BCTSH and BCTSH + Mn piezoelectric motors were the same as those used previously. It can be seen that the shaft of the BCTSH piezoelectric motors could not pull weights at a driving voltage of 200 V_{P-P}. This is attributed to three possible reasons for a motionless shaft: the weight of shaft, the weight of the load and the high driving AC voltage. These probably lead to heat generation in soft piezoelectric material, so working frequencies deviate from the resonant frequencies of the piezoelectric plate. The output of a piezoelectric motor decreases significantly. The shaft of the PZT-4 and BCTSH + Mn piezoelectric motors could pull weights upwards because the Q_m value was sufficiently large enough to vibrate the piezoelectric plates at a high driving voltage and there was a lower temperature rise, ΔT. The maximum upward speed, output force and output power for the PZT and BCTSH + Mn piezoelectric motors were 2.67 mm/s, 3.0 N and 2.5 mW and 2.56 mm/s, 2.5 N and 2.25 mW respectively. The formula for the displacement (D) of a piezoelectric plate at the resonant frequency is as follows:

$$D = \alpha \times d \times E \times L; \alpha = \beta \times Q_m \quad (6)$$

where α, and β are constant, Q_m is the mechanical quality factor and d is the piezoelectric charge constant.

If the thickness of piezoelectric plates and the electrical field are fixed, the displacement of the piezoelectric plate at the resonant frequency is proportional to the product of d and Q_m. Similar to the product of d_{33} and Q_m for soft and hard piezoelectric material in high-power piezoelectric motors, a high Q_m value for hard piezoelectric materials is more suitable than a high d_{33} value for soft piezoelectric materials with a low Q_m value. This is attributed to the fact that a high Q_m (low friction of domain wall) reduces heat generation, and a stable piezoelectric coefficient and resonant frequency is maintained, as discussed in the previous section.

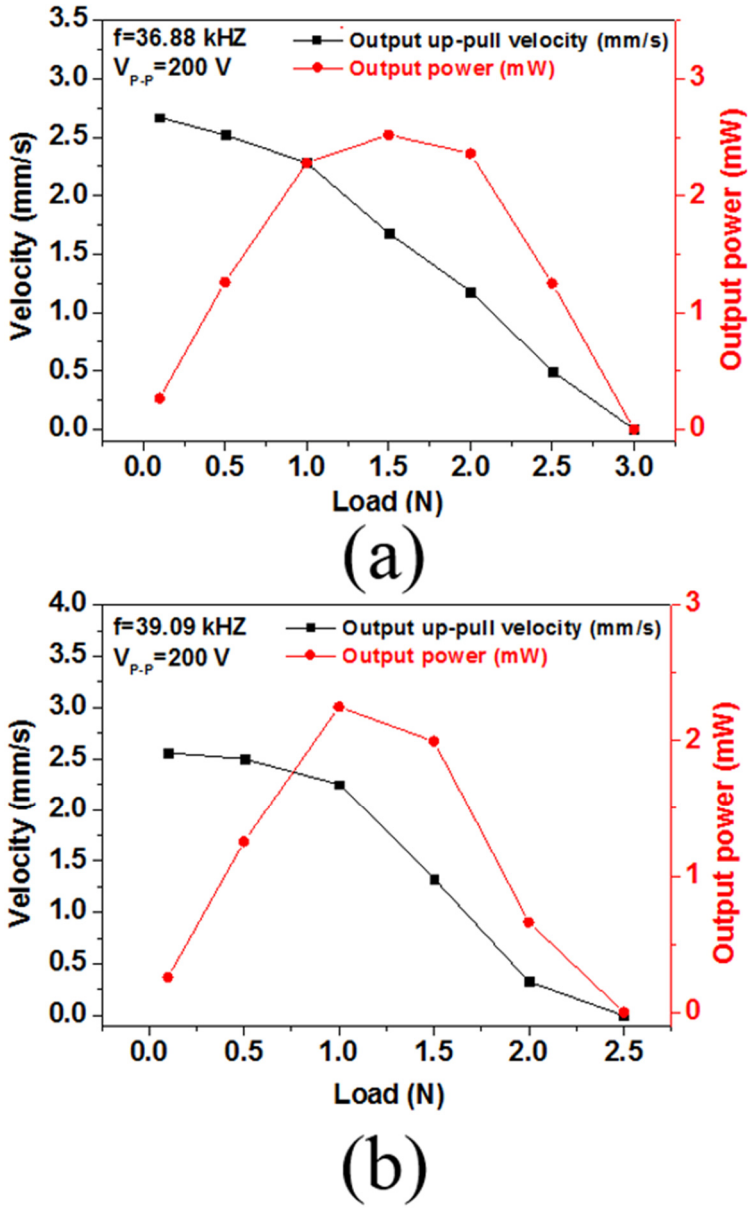

Figure 12. The relationship between the upward speed, force and output power for (**a**) PZT-4 and (**b**) BCTSH + Mn piezoelectric motors. The amplitude of the two–phase driving voltage was measured at their driving frequencies.

3.3. The Use of Lead-Free BCTSH + Mn Piezoelectric Motors to Pull a Commercial Insulin Syringe

Syringes are used to inject insulin, contrast agent and anesthetic. A miniature linear piezoelectric motor with a high driving frequency and a high resolution is a suitably precise driving device and an electromagnetic motor can be fabricated using the same structure and requirements for piezoelectric motors. Diabetics rely on insulin and glucagon to regulate their blood glucose level within a very narrow range by excluding it from the blood to most cells, such as muscles and adipose tissues, and turning it into energy in the human body. An excess or shortage of glucose in the blood leads to a metabolic disorder. The condition in which the glucose level in the blood is much higher than expected is called hyperglycemia. This symptom gives rise to drowsiness, nausea, tiredness and loss of consciousness, and eventually becomes diabetes in the long term [44]. It is important to control the dosage of insulin accurately.

Figure 13a–c show pictures of the leftward or rightward motion, upward motion and pulling a syringe using a squiggle motor. In this case, piezoelectric motors pull a commercial 0.5 mL insulin syringe. The front-, middle- and back-end speeds were 2.78 mm/s, 3.07 mm/s and 3.48 mm/s, respectively. Initially, the shaft in the motor must overcome a pressure difference, so the front speed was slow. Gradually, the speed increased linearly, until the shaft pulled the plunger up to the end of the syringe. The proposed BCTSH + Mn piezoelectric motors worked smoothly and kept at the resonant frequencies approximately constant for a period of time, so the forward speed of the BCTSH + Mn piezoelectric motors did not obviously decrease. The properties of the piezoelectric motor (rotary-linear ultrasonic motor) using the BCTSH + Mn ceramic sheets were compared with those using the PZT ceramic sheets.

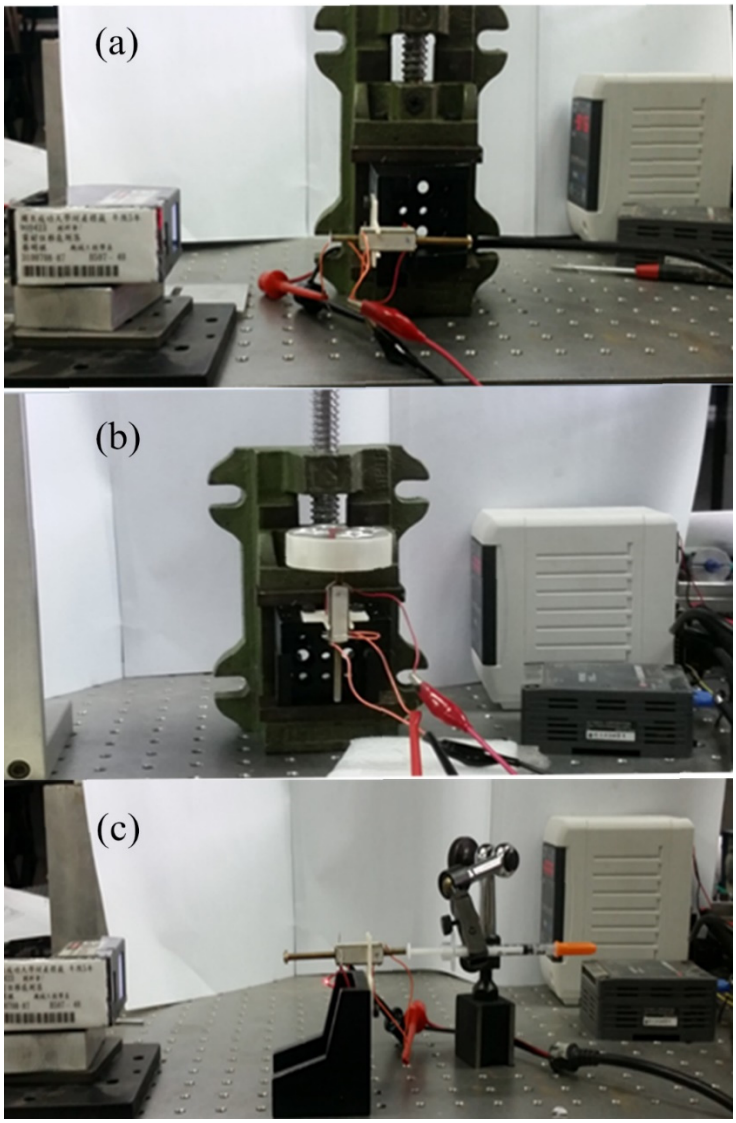

Figure 13. A picture of (**a**) the leftward or rightward motion for a squiggle motor, (**b**) the upward motion and (**c**) pulling a syringe using a squiggle motor.

4. Conclusions

In this paper, a rotary-linear ultrasonic motor's stator was excited by two electrical signals with a 90° phase difference. The piezoelectric parameters for the BCTSH + Mn ceramics were: k_p = 0.364, k_{31} = 0.49, d_{33} = 230 pC/N, d_{31} = −52 pC/N, Q_m = 340.8 and a microstructure of AGS = 22.59 μm. The output characteristics for the linear piezoelectric motor using BCTSH + Mn ceramic sheets at a driving voltage of 200 V_{P-P} and resonant fre-

quency of 39.09 kHz were: left-pull velocity = 3.21 mm/s, right-pull velocity = 3.39 mm/s, up-pull velocity = 2.56 mm/s and force >2 N, which are comparable to the output characteristics for linear piezoelectric motors using PZT ceramic sheets. This lead-free linear piezoelectric motor could pull a commercial 0.5 mL insulin syringe. The front-, middle- and back-end speeds were 2.78 mm/s, 3.07 mm/s and 3.48 mm/s, respectively.

Author Contributions: Conceptualization, designing, writing—original draft preparation: C.-C.T.; S.-Y.C. and W.-H.C. Writing—review and editing: C.-C.T. and S.-Y.C. Experimentation, analysis: W.-H.C. Simulation: C.-C.T.; S.-Y.C. and C.-S.H. Supervision, visualization: C.-S.H.; S.-Y.C. and C.-C.T. All authors have read and agreed to the published version of the manuscript.

Funding: We gratefully acknowledge the financial support provided from the Ministry of Science and Technology (MOST), Taiwan (Grant numbers: MOST 107-2221-E-272-002-, 107-2218-E006-035-, 108-2221-E-272-001-MY2).

Conflicts of Interest: The authors declare no conflict of interest.

References

1. Uchino, K. Piezoelectric ultrasonic motors: Overview. *Smart Mater. Struct.* **1998**, *7*, 273–285. [CrossRef]
2. Uchino, K. *Ferroelectric Devices*; Marcel Dekker, Inc.: New York, NY, USA, 2000.
3. Zhao, C.S. *Ultrasonic Motors Technologies and Applications*; Science Press: Beijing, China, 2007.
4. Watson, B.; Friend, J.; Yeo, L. Piezoelectric ultrasonic micro/milli-scale actuators. *Sens. Actuator. A Phys.* **2009**, *152*, 219–233. [CrossRef]
5. Siyuan, H.; Chiarot, P.R.; Park, S. A single vibration mode tubular piezoelectric ultrasonic motor. *IEEE Trans. Ultrason. Ferroelectr. Freq. Control* **2011**, *58*, 1049–10611. [CrossRef]
6. Delibas, B.; Koc, B. A Method to Realize Low Velocity Movability and Eliminate Friction induced Noise in Piezoelectric Ultrasonic Motors. *IEEE/ASME Trans. Mechatro. Mechatron.* **2020**, *25*, 2677–2687. [CrossRef]
7. Tian, X.; Liu, Y.; Deng, J.; Wang, L.; Chen, W. A review on piezoelectric ultrasonic motors for the past decade: Classification, operating principle, performance and future work perspectives. *Sens. Actuator A Phys.* **2020**, *306*, 111971. [CrossRef]
8. Mizuno, A.; Kajiwara, H.; Tamura, H.; Aoyagi, M.M. Study on Multidegree-of-Freedom Ultrasonic Motor Using Vibration Mode Rotation of Metal Spherical Stator. *Actuator* **2022**, *11*, 27. [CrossRef]
9. Williams, A.L.W.; Brown, W.J. Piezoelectric Motor. U.S. Patent 2,439,499, 13 April 1948.
10. Henderson, D.A. Simple Ceramic Motor. Inspiring Smaller Products. In Proceedings of the 10th International Conference on New Actuators, Bremen, Germany, 14–16 June 2006; Volume 50, pp. 1–4.
11. Ali, W.G.; Nagi, G. Embedded Control Design for Insulin Pump. *Adv. Mater. Res.* **2011**, *201–203*, 2399–2404. [CrossRef]
12. Henderson, D. Novel piezo motor enables positive displacement microfluidic pump. *New Scale Technol.* **2007**, *3*, 272–275.
13. Jaffe, B.; Cook, W.R.; Jaffe, H. *Piezoelectric Ceramics*; Academic Press: London, UK; New York, NY, USA, 1971.
14. Saito, Y.; Takao, H.; Tani, T.; Nonoyama, T.; Takatori, K.; Homma, T.; Nagaya, T.; Nakamura, M.M. Lead-Free Piezoceramics. *Nature* **2004**, *432*, 84–87. [CrossRef]
15. Rödel, J.; Jo, W.; Seifert, K.; Anton, E.M.; Granzow, T.; Damjanovic, D. Perspective on the Development of Lead-Free Piezoceramics. *J. Am. Ceram. Soc.* **2009**, *92*, 1153–1157. [CrossRef]
16. Du, H.; Li, Z.; Tang, F.; Qu, S.; Pei, Z.; Zhou, W. Preparation and Piezoelectric Properties of $(K_{0.5}Na_{0.5})NbO_3$ Lead-Free Piezoelectric Ceramics with Pressure-Less Sintering. *Mater. Sci. Eng. B* **2006**, *131*, 83–87.
17. Kantha, P.; Pengpat, K.; Jarupoom, P.; Intatha, U.; Rujijanagul, G.; Tunkasiri, T. Phase Formation and Electrical Properties of BNLT–BZT Lead-Free Piezoelectric Ceramic System. *Curr. Appl. Phys.* **2009**, *9*, 460–466. [CrossRef]
18. Zhang, Y.; Li, J.; Zhang, B.; Peng, C. Piezoelectric and Ferroelectric Properties of Bi-Compensated $(Bi_{1/2}Na_{1/2})TiO_3$-$(Bi_{1/2}K_{1/2})TiO_3$ Lead-Free Piezoelectric Ceramics. *J. Appl. Phys.* **2008**, *103*, 074109. [CrossRef]
19. Zhou, C.; Liu, X. Effect of B-Site Substitution of Complex Ions on Dielectric and Piezoelectric Properties in $(Bi_{1/2}Na_{1/2})TiO_3$ Piezoelectric Ceramics. *Mater. Chem. Phys.* **2008**, *108*, 413–416. [CrossRef]
20. Zhou, X.; Xue, G.; Luo, H.; Bowen, C.R.; Zhang, D. Phase structure and properties of sodium bismuth titanate lead-free piezoelectric ceramics. *Prog. Mater. Sci.* **2021**, *122*, 100836. [CrossRef]
21. Liu, W.; Ren, X. Large Piezoelectric Effect in Pb-Free Ceramics. *Appl. Phys. Lett.* **2009**, *103*, 257602. [CrossRef] [PubMed]
22. Wu, J.; Wang, Z.; Zhang, B.; Zhu, J.; Xiao, D. $Ba_{0.85}Ca_{0.15}Ti_{0.90}Zr_{0.10}O_3$ Lead-free Ceramics with a Sintering Aid of MnO. *Integr. Ferroelectr.* **2013**, *141*, 89–98. [CrossRef]
23. Zhang, Y.; Xie, M.; Roscow, J.; Bowen, C. Dielectric and piezoelectric properties of porous lead-free $0.5Ba(Ca_{0.8}Zr_{0.2})O_3$-$0.5(Ba_{0.7}Ca_{0.3})TiO_3$ ceramics. *Mater. Res. Bull.* **2019**, *112*, 426–431. [CrossRef]
24. Xue, D.; Zhou, Y.; Bao, H.; Gao, J.; Zhou, C.; Ren, X. Large Piezoelectric Effect in Pb-free Ba(Ti,Sn)O-x(Ba,Ca)TiO_3 Ceramics. *Appl. Phys. Lett.* **2011**, *99*, 122901. [CrossRef]

25. Zhou, P.F.; Zhang, B.P.; Zhao, L.; Zhu, L.F. Effect of LiF addition on phase structure and piezoelectric propertiesof (Ba,Ca)(Ti,Sn)O_3 ceramics sintered at low temperature. *Ceram. Int.* **2015**, *41*, 4035–4041. [CrossRef]
26. Zhao, L.; Zhang, B.P.; Zhou, P.F.; Zhu, L.F.; Li, J.F. Effect of Li_2O Addition on Sintering and Piezoelectric Properties of (Ba,Ca)(Ti,Sn)O_3 Lead-Free Piezoceramics. *J. Eur. Ceram. Soc.* **2015**, *35*, 533–540. [CrossRef]
27. Zhou, P.F.; Zhang, B.P.; Zhao, L.; Zhao, X.K.; Zhu, L.F.; Cheng, L.Q. High Piezoelectricity Due to Multiphase Coexistence in Low-Temperature Sintered (Ba,Ca)(Ti,Sn)O_3–CuOx Ceramics. *Appl. Phys. Let.* **2013**, *103*, 172904. [CrossRef]
28. Wu, B.; Xiao, D.; Wu, J.J.; Huang, T.; Wang, Z.; Liu, C.; Li, F.; Zhu, J. Microstructures and Piezoelectric properties of CuO-doped ($Ba_{0.98}Ca_{0.02}$)($Ti_{0.94}Sn_{0.06}$)O_3 ceramics. *J. Electroceram.* **2014**, *33*, 117–120. [CrossRef]
29. Zhao, C.; Feng, Y.; Wu, H.; Wu, J. Phase boundary design and high piezoelectric activity in (1-x)($Ba_{0.93}Ca_{0.07}$)TiO_3-x$Ba(Sn_{1-y}Hf_y)O_3$ lead-free ceramics. *J. Alloy. Compd.* **2016**, *66*, 372–379.
30. Jin, J.; Wan, D.; Yang, Y.; Li, Q.; Zha, M. A linear ultrasonic motor using ($K_{0.5}Na_{0.5}$)NbO_3 based lead-free piezoelectric ceramics. *Sens. Actuators A Phys.* **2011**, *165*, 410–414. [CrossRef]
31. Li, E.; Kakemoto, H.; Hoshina, T.; Tsurumi, T. A Shear-Mode Ultrasonic Motor Using Potassium Sodium Niobate-Based Ceramics with High Mechanical Quality Factor. *Jap. J. Appl. Phys.* **2008**, *47*, 7702–7706. [CrossRef]
32. Doshida, Y.; Kishimoto, S.; Irieda1, T.; Tamura, H.; Tomikawa, Y.; Hirose, S. Miniature Ultrasonic Motor Using Shear Mode of Potassium Sodium Niobate-Based Lead-Free Piezoelectric Ceramics. *Jap. J. Appl. Phys.* **2008**, *45*, 09KD11.
33. Li, E.; Sasaki, R.; Hoshina, T.T.; Takeda, H.; Tsurumi, T. Double-Mode Miniature Cantilever-Type Ultrasonic Motor Using Lead-Free Array-Type Multilayer Piezoelectric Ceramics. *Jap. J. Appl. Phys.* **2009**, *47*, 4242–4247.
34. Tsai, C.C.; Chao, W.H.; Chu, S.Y.; Hong, C.S.; Weng, C.M.; Su, H.H. Enhanced temperature stability and quality factor with Hf substitution for Sn and MnO_2 doping of ($Ba_{0.97}Ca_{0.03}$)($Ti_{0.96}Sn_{0.04}$)O_3 lead-free piezoelectric ceramics with high Curie temperature. *AIP Adv.* **2016**, *6*, 125024. [CrossRef]
35. Jiang, X.P.; Li, L.; Chen, C.; Wang, X.J.; Li, X.H. Effects of Mn-Doping on the Properties of ($Ba_{0.92}Ca_{0.08}$)($Ti_{0.95}Zr_{0.05}$)O_3 Lead-Free Ceramics. *J. Alloys Compd.* **2013**, *574*, 88–91. [CrossRef]
36. Zheng, M.; Hou, Y.; Zhu, M.; Zhang, M.; Yan, H. Shift of Morphotropic Phase Boundary in High-Performance Fine-Grained PZN–PZT Ceramics. *J. Eur. Ceram. Soc.* **2014**, *34*, 2275–2283. [CrossRef]
37. Jiansirisomboon, S.; Watcharapasorn, A. Effects of alumina nano-particulates addition on mechanical and electrical properties of barium titanate ceramics. *Curr. Appl. Phys.* **2008**, *8*, 48–52. [CrossRef]
38. Kalyani, A.K.; Brajesh, K.; Senyshyn, A.; Ranjan, R. Orthorhombic-Tetragonal Phase Coexistence and Enhanced Piezo-Response at Room Temperature in Zr, Sn, and Hf Modified $BaTiO_3$. *Appl. Phys. Lett.* **2014**, *104*, 252906. [CrossRef]
39. Bhattacharya, K.; Ravichandran, G. Ferroelectric perovskites for electromechanical actuation. *Acta Mater.* **2003**, *51*, 5941–5960. [CrossRef]
40. Zhang, S.T.; Kounga, A.B.; Jo, W.; Jamin, C.; Seifert, K.; Granzow, T.; Roedel, J.; Damjanovic, D. High-Strain Lead-free Antiferroelectric Electrostrictors. *Adv. Mater.* **2009**, *21*, 4716–4720. [CrossRef]
41. Zuo, R.Z.; Fu, J.; Yin, G.Z.; Li, X.L.; Jiang, J.Z. Electric field induced phase instability in typical (Na,K)(Nb,Sb)O_3-$LiTaO_3$ ceramics near orthorhombic and tetragonal phase boundary. *Appl. Phys. Lett.* **2012**, *101*, 092906. [CrossRef]
42. Lebrun, L.; Petit, L.; Gonnard, P. Piezoelectric motor using a (1,1) non-axisymmetric mode. *Ultrasonics* **1996**, *34*, 251–255. [CrossRef]
43. Lebrun, L.; Petit, L.; Briot, R.; Gonnard, P. Electromechanical conversion in an ultrasonic motor using a non-axisymmetric (1,1) mode. *Smart Mater. Struct.* **2007**, *6*, 47–52. [CrossRef]
44. Blood Sugar, Wikipedia, the Free Encyclopedia. Available online: http://en.wikipedia.org/wiki/blood_sugar (accessed on 1 January 2022).